

## Research Article

# Investigation on the Deformation and Failure Characteristics of Shale Samples Containing Circular Hole considering the Bedding Angle Effect under Uniaxial Compression

Qinyuan Liang,<sup>1</sup> Cheng Zhao,<sup>2</sup> Yu Zhou ,<sup>1</sup> Bo Li,<sup>1,2</sup> and Ruyi Bao<sup>1</sup>

<sup>1</sup>Key Laboratory of Rock Mechanics and Geohazards of Zhejiang Province, Shaoxing University, Shaoxing, Zhejiang 312000, China

<sup>2</sup>Department of Geotechnical Engineering College of Civil Engineering, Tongji University, Shanghai 200092, China

Correspondence should be addressed to Yu Zhou; [zhouyu@usx.edu.cn](mailto:zhouyu@usx.edu.cn)

Received 7 January 2022; Accepted 7 February 2022; Published 7 March 2022

Academic Editor: Fuqiang Ren

Copyright © 2022 Qinyuan Liang et al. This is an open access article distributed under the Creative Commons Attribution License, which permits unrestricted use, distribution, and reproduction in any medium, provided the original work is properly cited.

The drilling and blasting method (DBM) is widely used in the excavation of tunnel engineering, and it is essential to first drill circular holes. This paper experimentally explored the influence of bedding angles on crack propagation of shale containing a circular hole. Specifically, the uniaxial compression tests were carried out on shale samples with a single prefabricated hole combined with digital image correlation technology (DIC) to obtain the real-time deformation process near the macro damage. The results show that the peak strength, global shear strain field, failure mode around the circular hole and macro crack failure mode of shale with prefabricated circular hole are closely related to the bedding dip angle. The strength generally increases with the decrease of the bedding angle. Two transitions of failure mode were observed at the point of 45° and 75°: tensile shear mixed failure around the circular hole (less than 45°) first transits into no damage around the circular hole (60° and 70°), and then, tensile failure occurs around the circular hole (90°). In addition, for the cases of 60° and 75°, tensile failure away from the circular hole occurs along the weak surface of bedding, while for the other cases, the tensile failure through the circular hole mainly occurs. These findings have implied that the bedding angle is one essential parameter that needs to be considered for the stability of tunnel surrounding rock.

## 1. Introduction

Compared with traditional rock crushing mechanical methods (tunnel boring machines, rock breakers), the drilling and blasting method (DBM) has the advantage of low initial investment and cheap explosive energy and the possibility to construct openings with different shapes and sizes, so it is widely used in tunnel excavation [1–4]. To bury explosives, the DBM method usually needs to drill round holes, then clean the holes, and bury explosives for initiation excavation [5, 6]. However, on the one hand, the manually drilled holes can change the mechanical properties of the rock. On the other hand, due to unavoidable factors, the site selection of the tunnel must cross the active fault zone, where the geological structure is strong, and the manually drilled

holes are easy to induce engineering geological disasters. Therefore, it is of great significance to study the deformation and crack propagation law of hole rock for the stability of tunnel surrounding rock [7–17].

At present, the researches on the mechanical response of rock materials with prefabricated voids mainly focus on exploring the crack initiation, propagation, and penetrating. Wong et al. [18] have carried out a series of experimental and numerical uniaxial compression tests on granite samples containing a single hole with different sizes of hole and granite samples to study the influence of hole on the failure modes and strength characterizations. It was found that cracks generated near the holes do not seem to tend to extend towards the free boundary, while first propagating outward from the free boundary and then parallel to the free

boundary, resulting in buckling failure. Li et al. [19] studied the influence of preformed holes with different geometries (i.e., size, shape, and angles) on the strength and fracture behaviour of marble using digital image correlation (DIC). It was found that the propagation of tensile cracks around the holes was mainly affected by the nucleation and propagation of cracks in the strain localization zone. Fan et al. [20] carried out a uniaxial compression test of sandstone with a single hole. The results showed that the hole significantly disturbed the internal stress distribution of the hole wall and internal stress was always intensively distributed at both sidewalls of the hole, especially at the midpoint of sidewalls; therefore, the spalling of rock cuttings on the sidewall can be first observed. Wang et al. [21–23] carried out experimental and numerical simulation studies under multiaxial stress conditions with the help of transparent resin materials containing spherical voids. It was found that the main feature of three-dimensional crack propagation under uniaxial compression is the formation of wing cracks wrapped around the initial circular hole. In biaxial compression, the shape of three-dimensional crack propagation is qualitatively affected by the intermediate principal stress. When the intermediate principal stress is relatively low, a large wing crack will also be formed, and its propagation degree is enough to split the sample. Based on DIC and wave velocity tests, Han et al. [24] studied the effect of hole size on the deformation and failure of 90° shale. The results found that large hole diameter (10 mm) and medium hole diameter (6 mm) were dominated by tensile failure, while a small hole diameter (2 mm) exhibited mixed tension and shear failure.

Many scholars have selected granite, marble, sandstone, and rock-like materials as their research objects to study the influence of prefabricated cavities on the deformation and crack propagation laws of rock materials, but few works have considered the influence of cavities on shale with different bedding angles. However, in tunnel engineering, shale is one common surrounding rock material [25, 26]. Because of its obvious layered structure, it shows significant anisotropy, which seriously affects the safety and stability of the tunnel [27–29]. Given this, domestic and foreign scholars have developed the law of the influence of bedding dip on the mechanical behaviour of intact shale. Niandou et al. [30] summarized the failure modes of shale under compressive load into three categories, namely, bedding plane sliding failure mode, sliding failure mode, and shear zone failure mode. Zhang et al. [31] conducted uniaxial compression tests on shales in Western Hubei and Eastern Chongqing with different bedding plane angles and found that the failure mode varies with bedding plane angles: the tensile failure dominates at 0° and 90°, while the failure mode is mainly shear failure when the loading direction is at a certain angle with the bedding plane, that is, 22.5°, 45°, and 67.5°. Hou et al. [29] conducted SEM and uniaxial compression test on shale with different bedding angles and found that the uniaxial compressive strength curve was approximately in the shape of “U”: the maximum values occur with the shale bedding angles of 0° and 90°, and the minimal value is 30°. Yin et al. [32] summarized eight factors affecting UCS of shale and concluded that the bedding plane has a significant

impact. Zhang et al. [33] studied the anisotropic characteristics of mechanical parameters of shale through uniaxial compression of shale with different bedding angles. It was found that with the gradual increase of bedding angle, the uniaxial compression strength curve exhibits a common “U” shape.

To date, the existing research systematically analyzes the influence law of bedding dip angle on the mechanical behaviour of intact shale, but less work considers the influence caused by the existence of holes. This paper took shale with different bedding angles as the research object and conducted uniaxial compression tests on shale samples with a prefabricated circular hole. With the help of digital image correlation (DIC), the changes in the global strain field during sample loading were monitored. The influence of bedding dip angle on the crack propagation law of shale with a circular hole was discussed, to further provide some technical support for the safety and stability of surrounding rock in tunnel engineering.

## 2. Test Preparation

**2.1. Sample Preparation.** The rock samples used in the test were collected from Changning County, Yibin City, Sichuan Province. The rocks in this section belong to the shale of the long-1 submember of the formation of the Lower Silurian system. To explore the influence of bedding dip angle on the crack propagation law of shale with a single circular hole, the rectangular plate samples (150 × 75 × 20 mm) with the included angles between bedding plane and horizontal lines of 0°, 15°, 30°, 45°, 60°, 75°, and 90° were prepared (as shown in Figure 1). To simulate the blast hole in DBM, the prefabricated single circular hole with a diameter of 6 mm is drilled in the geometric centre of the samples using a glass bit. To reduce individual differences, the above samples are prepared and processed from the same rock block. Before the DIC test begins, considering the natural black appearance of the shale, white paint of the Tamiya brand was sprayed on the surface to form random black and white speckles.

### 2.2. Introduction to DIC and Test

**2.2.1. Introduction to DIC.** The basic idea of the digital image correlation method is to quantify the specific subdomains before and after the deformation of the sample, to obtain the full-field deformation and strain of the sample. Assuming that the image grayscale eigenvalue functions before and after deformation of the sample are  $f_1(x, y)$  and  $f_2(x', y')$ , respectively, and the object displacement field functions are  $u(x, y)$  and  $v(x, y)$ . Then, the coordinates before and after image deformation are  $(x, y)$  and  $(x', y')$ , and the relationship is

$$\begin{aligned}x' &= x + u(x, y), \\y' &= y + v(x, y).\end{aligned}\tag{1}$$

To evaluate the similarity between the reference image and the current image, it is necessary to compare the grey

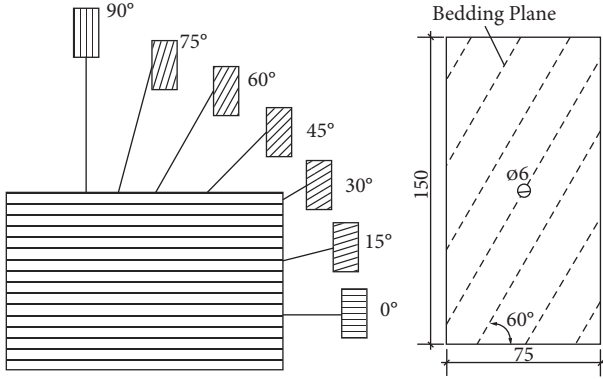


FIGURE 1: Schematic diagram of bedding angle of samples.

values between the two images and introduce the correlation coefficient  $C$  to represent the similarity between the current image after deformation and the reference image without deformation.

$$C = \frac{\sum[f_1(x, y) - f_{1m}] \times [f_2(x', y') - f_{2m}]}{\sqrt{\sum[f_1(x, y) - f_{1m}]^2} \sqrt{\sum[f_2(x', y') - f_{2m}]^2}}, \quad (2)$$

where  $f_1(x, y)$  and  $f_2(x', y')$  are the grey eigenvalue functions of the image before and after the deformation, and  $f_{1m}$  and  $f_{2m}$  are the grey mean values of the subregions of the image before and after the deformation. The range of correlation coefficient  $C$  is in the range of 0–1. The smaller the correlation coefficient  $C$  is, the more irrelevant the two subdomains are; the larger the correlation coefficient  $C$  is, the more relevant the two subdomains are. In general, when correlation coefficient  $C$  is at its maximum value, the operator region is the target subregion. The global displacement field can be obtained by calculating different subdomains. According to the global displacement field, the global strain field can be calculated by the Cauchy equation. This is the basic principle of digital image technology to obtain object displacement and strain fields [34].

**2.2.2. DIC Test.** The test equipment (Figure 2) consists of a loading system, observation system, and analysis system. The loading system adopts servo-hydraulic control, and its maximum loading force is 600 kN. To weaken the end effect, the vaseline was smeared on the upper and lower ends of the sample before loading. The displacement control mode is adopted in the test with a loading velocity of 0.2 mm/min. The observation system consists of halogen lamps arranged on both sides of the sample and a set of the high-speed camera system to capture the real-time image of crack incubation and evolution during loading. 300 original images shall be taken before loading, and the post-trigger mode shall be opened during loading at 600 frames per second. Finally, the global strain field can be measured based on the open-access Ncorr software [35]. Unless otherwise stated, the calculation parameters used herein are shown in Table 1.

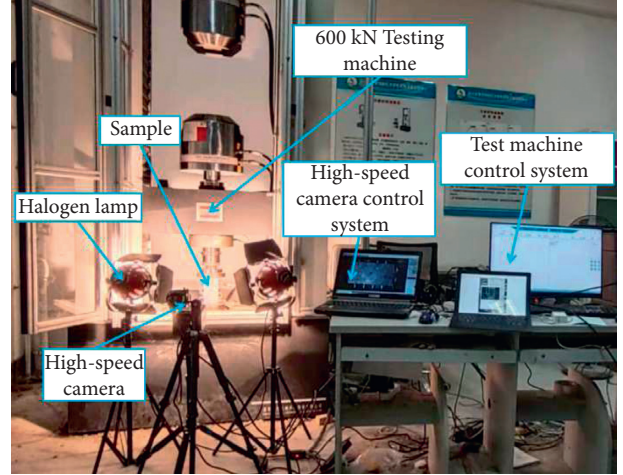


FIGURE 2: Test equipment.

TABLE 1: Main calculation parameters used in Ncorr.

Subset radius	Subset spacing	Difference vector cutoff	Strain radius
20 pixels	0	1.00E-08	5 pixels

### 3. Test Results and Discussion

**3.1. Uniaxial Compressive Strength.** Figure 3 shows the relationship between uniaxial compressive strength and bedding angle of shale with prefabricated circular holes. It can be seen that the uniaxial compressive strength generally shows a downward trend with the increase of bedding angle. The compressive strength of the 15° sample is the largest, and the uniaxial compressive strength is 147.12 MPa. The uniaxial compressive strength of 30°, 45°, 60°, and 75° specimens decreases gradually with the increase of bedding dip angle. Among them, the uniaxial compressive strength of the 75° specimen is the smallest, and the test value is 40.78 MPa. The peak strength of 90° bedding is 3.37 MPa higher than that of 75° bedding. This is different from the results of Zhang et al. [31], He et al. [36], and Xie et al. [37] (the uniaxial compressive strength is the smallest when the bedding angle is 50°, 60°, and 45°, respectively). The mechanisms behind this phenomenon are as follows: on the one hand, the mechanical properties of shales in different regions are different [33]; on the other hand, it is significantly affected by the prefabricated circular hole set in the geometric centre of shale, which will be discussed in the following section.

According to the test, the variation trend of uniaxial compressive strength of shale with prefabricated circular holes with bedding dip angle is obtained, and the fitting curve is as follows:

$$\sigma_c = 0.00035\theta^3 - 0.03562\theta^2 - 0.7469\theta + 149.31139, \quad (3)$$

where  $\sigma_c$  is uniaxial compressive strength;  $\theta$  is the angle between bedding and horizontal plane.

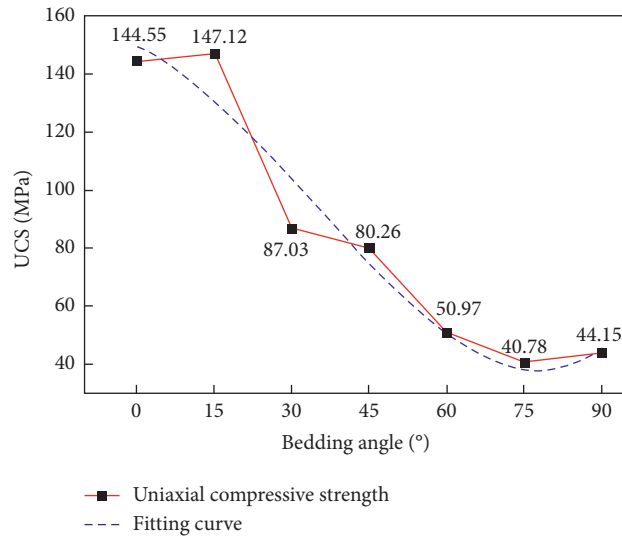


FIGURE 3: Relationship between uniaxial compressive strength and bedding angle.

**3.2. Deformation and Failure Characteristics.** To explore the influence of bedding dip angle on crack propagation of shale with a circular hole, the global strain field evolution at the moment of shale failure is quantitatively analyzed by using the digital image correlation method. What should be noted is that, for the case of 75°, a large area of the spalling area appears along the weak bedding surface at the upper right of the test surface, resulting in the lack of speckle data; thus, the global strain field cannot be captured and has not been listed. Given this, this paper only analyzes the strain of shale samples with prefabricated circular holes at 0°, 15°, 30°, 45°, 60°, and 90° and obtains the cloud charts of tensile strain field evolution and shear strain field evolution (as shown in Figures 4–15). The  $t$  value represents the time before fracturing.

As can be seen from Figures 4 and 5, for the specimen with a bedding angle of 0°, a tensile concentrated strain region appears at the upper left, and the value of the shear strain field corresponding to this region is large. Therefore, it can be judged that the macro crack at the upper left is a tensile shear failure. A tensile strain concentration area passes through the circular hole and gradually expands along the compressive stress direction. When it tends to fail, the shear strain concentration appears near the circular hole. Therefore, it can be judged that the macro crack passing through the circular hole is dominated by tensile failure, while the mixed failure is dominated around the circular hole.

By observing the tensile strain field in Figures 6 and 7, it can be seen that for the sample with an angle of 15°, at 5000 ms, the crack initiates at the upper part of the circular hole. At 3000 ms, the tensile strain concentration area also occurs at the upper right of the circular hole. As loading time increases, the tensile strain concentration area gradually extends along the loading direction. Two independent cracks finally merge on the right side of the circular hole, and then, instability failure occurs. By observing the shear strain field, it can be found that the global shear strain of the sample is

large, and there is a shear strain concentration area around the circular hole. Therefore, it can be judged that the macro crack through the circular hole is dominated by tensile failure, and the failure around the circular hole is dominated by tensile shear mixed failure. Combined with the peak strength date, when the bedding dip angle is 0° and 15°, that is, the loading direction and bedding dip angle are large, the mixed failure of bedding plane and shale matrix occurs. At this time, the peak strength largely depends on the shale matrix itself, reflecting the compressive capacity of the shale matrix.

It can be found that when the bedding angle reaches 30° (shown in Figures 8 and 9), the macro crack penetrating the circular hole is mainly dominated by tensile failure, and the global shear strain of the sample is large. With the bedding angle further increasing to 45° (Figures 10 and 11), the spalling failure occurs at the upper right end of the sample, the macro crack through the circular hole is dominated by tensile failure, and the global shear strain of the sample is large. By comprehensively comparing the 30° and 45° strain fields, the cementation of bedding planes with weak strength begins to significantly affect the deformation process of rock. In particular, when the bedding dip angle is 45°, a local concentration area of tensile strain is generated along the bedding angle, and as loading time increases, the local area of tensile strain slides along the bedding angle and finally runs through the weak bedding plane, resulting in rock instability and failure. Therefore, the uniaxial compressive strength decreased significantly.

Figures 12 and 13 show the cloud charts of tensile strain field and shear strain field evolution of the sample with a bedding angle of 60°, respectively. A tensile concentrated strain zone is generated at the upper right side of the sample and extends to the outside of the sample in the direction of approximately 60°, while the shear one is relatively homogeneous. Therefore, it can be judged that the macro crack is tensile (the failure mode of the sample with a bedding angle of 75° is similar to that of 60°).

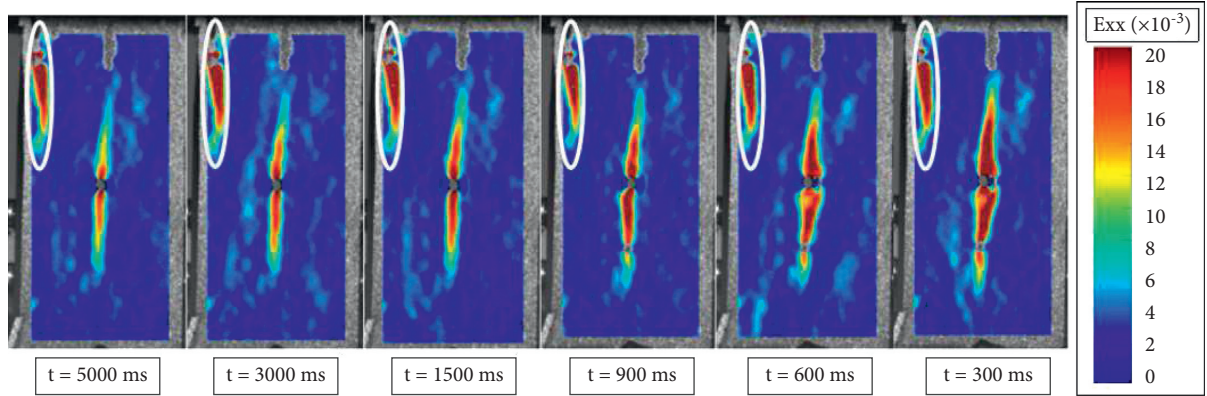


FIGURE 4: Cloud charts of tensile strain field evolution of shale sample with bedding angle of  $0^\circ$  (where red represents tensile strain, blue represents compressive strain).

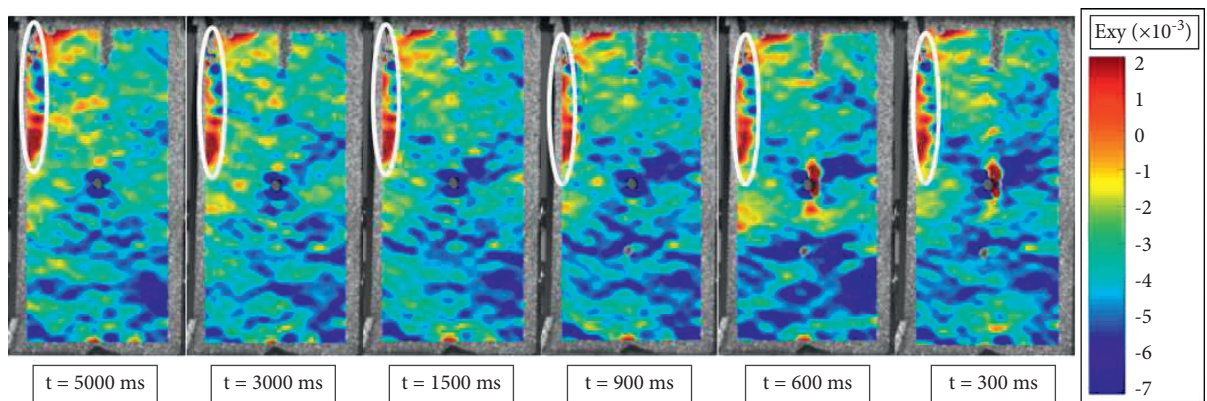


FIGURE 5: Cloud charts of shear strain field evolution of shale sample with hole bedding angle of  $0^\circ$  (where the  $t$  value represents the time before fracturing, red represents positive shear strain and blue represents negative shear strain).

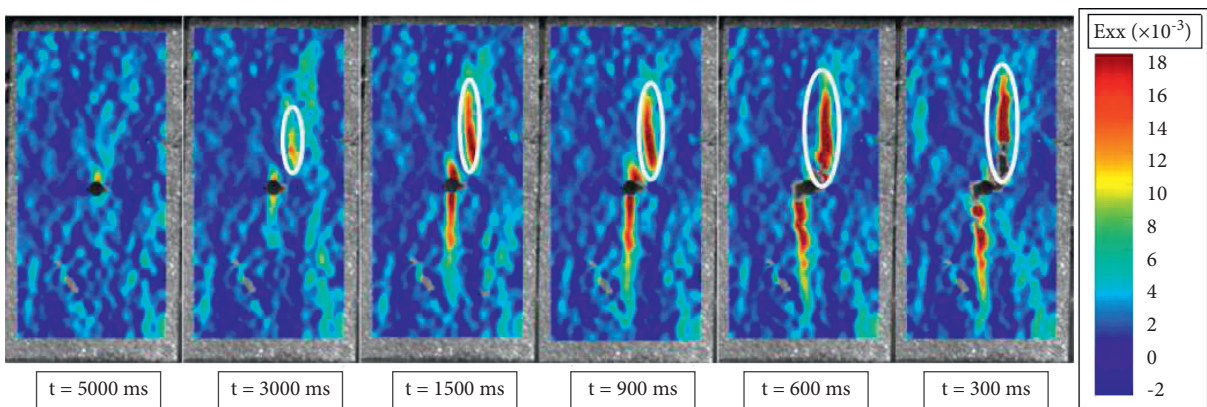


FIGURE 6: Cloud charts of tensile strain field evolution of shale sample with bedding angle of  $15^\circ$  (where the  $t$  value represents the time before fracturing, red represents tensile strain and blue represents compressive strain).

Observing the strain field of the  $90^\circ$  specimens shown in Figures 14 and 15, it can be found that a vertical tensile strain concentration zone penetrating a circular hole is first generated in the centre of the shale, and then, a short vertical tensile strain concentration zone appears on the upper right side of the specimens, both of which are parallel to the shale bedding angle. Since the loading direction is parallel to the bedding

plane and the bedding plane is in a tension state, a vertical tension strain concentration zone is generated. Therefore, the peak strength largely depends on the strength of the bedding plane, reflecting the compressive capacity of the bedding plane. In summary, it can be inferred that when the bedding dip angle is greater than  $45^\circ$ , the specimen will slip along the weak plane of bedding, and the peak strength is small.

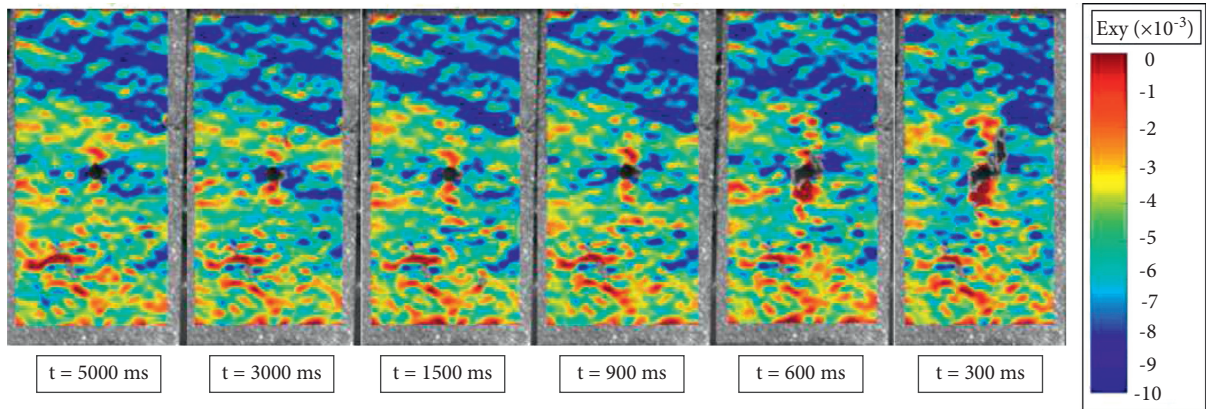


FIGURE 7: Cloud charts of shear strain field evolution of shale sample with hole bedding angle of  $15^\circ$  (where the  $t$  value represents the time before fracturing, red represents positive shear strain and blue represents negative shear strain).

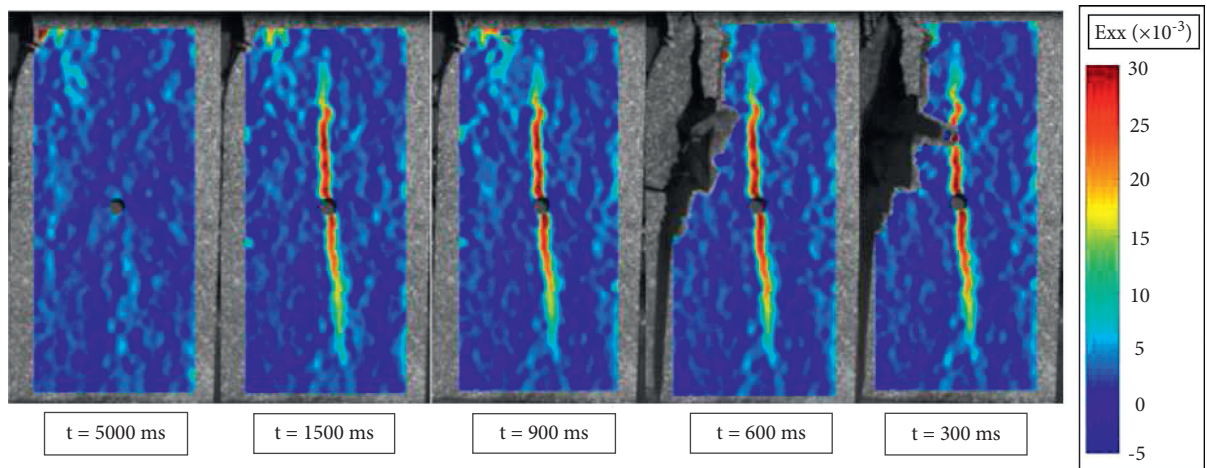


FIGURE 8: Cloud charts of tensile strain field evolution of shale sample with bedding angle of  $30^\circ$  (where the  $t$  value represents the time before fracturing, red represents tensile strain and blue represents compressive strain).

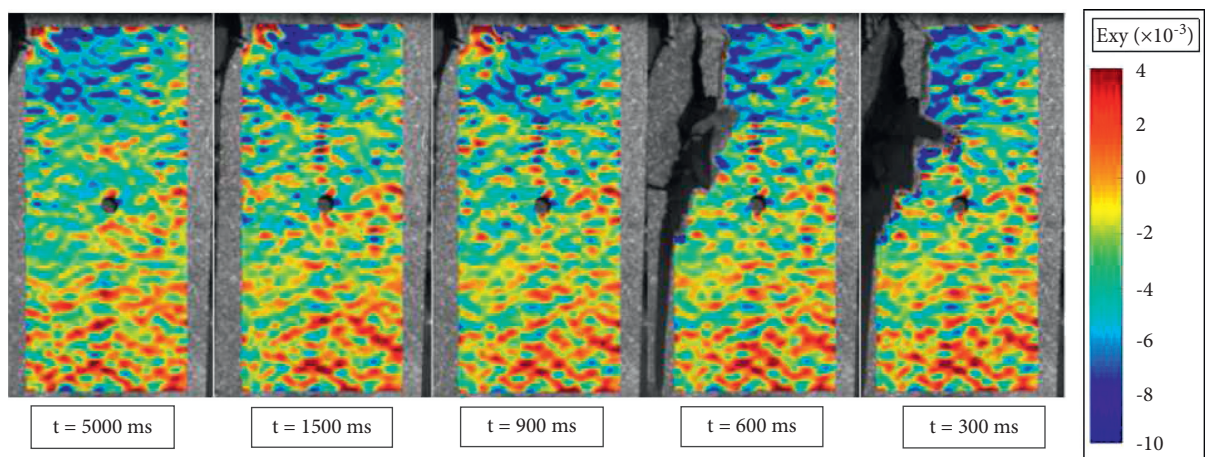


FIGURE 9: Cloud charts of shear strain field evolution of shale sample with hole bedding angle of  $30^\circ$  (where the  $t$  value represents the time before fracturing, red represents positive shear strain and blue represents negative shear strain).

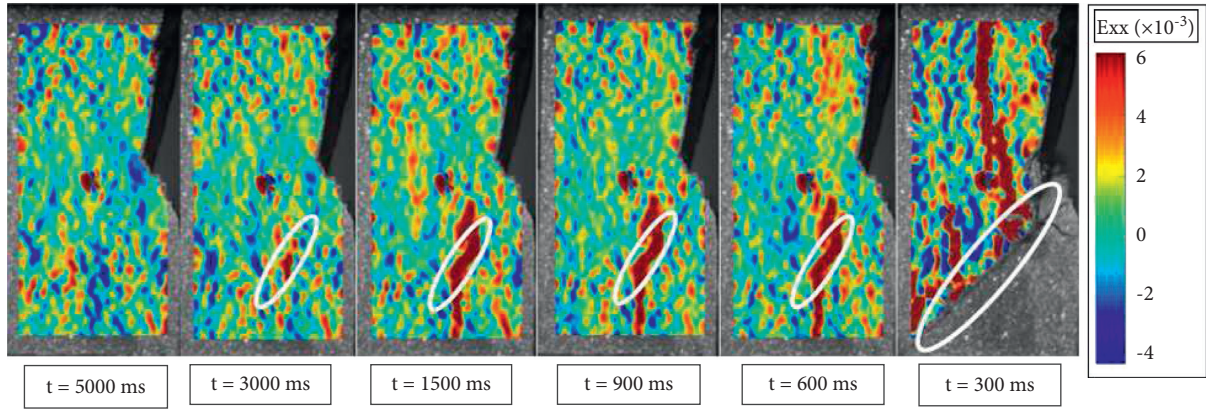


FIGURE 10: Cloud charts of tensile strain field evolution of shale sample with bedding angle of  $45^\circ$  (where the  $t$  value represents the time before fracturing, red represents tensile strain and blue represents compressive strain).

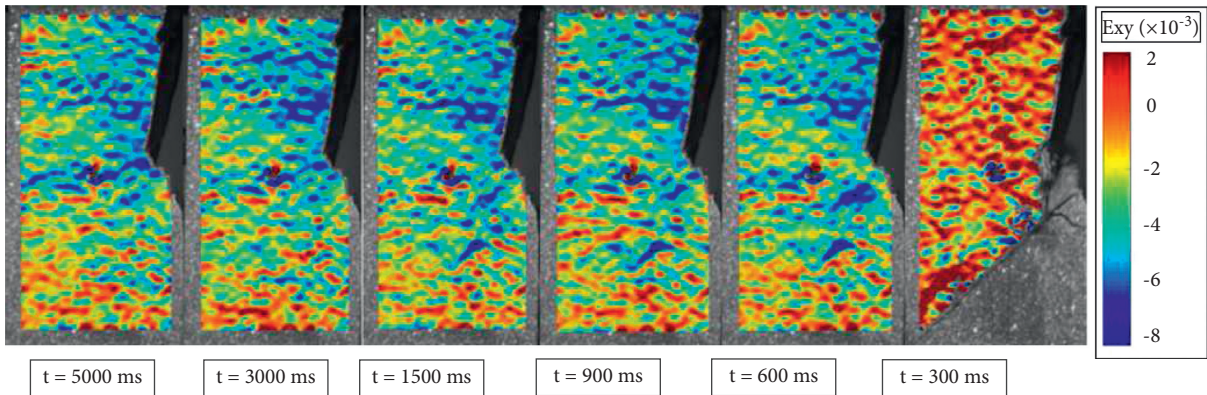


FIGURE 11: Cloud charts of shear strain field evolution of shale sample with hole bedding angle of  $45^\circ$  (where the  $t$  value represents the time before fracturing, red represents positive shear strain and blue represents negative shear strain).

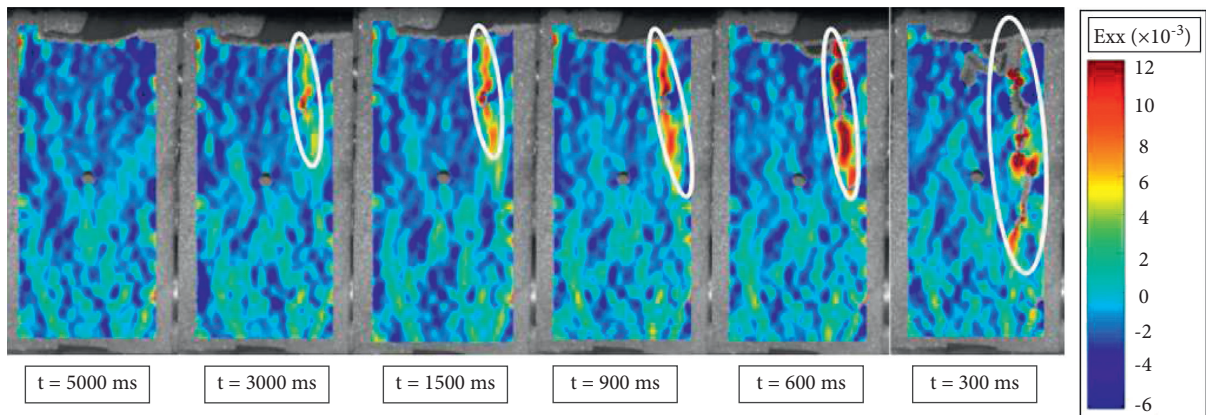


FIGURE 12: Cloud charts of tensile strain field evolution of shale sample with bedding angle of  $60^\circ$  (where the  $t$  value represents the time before fracturing, red represents tensile strain and blue represents compressive strain).

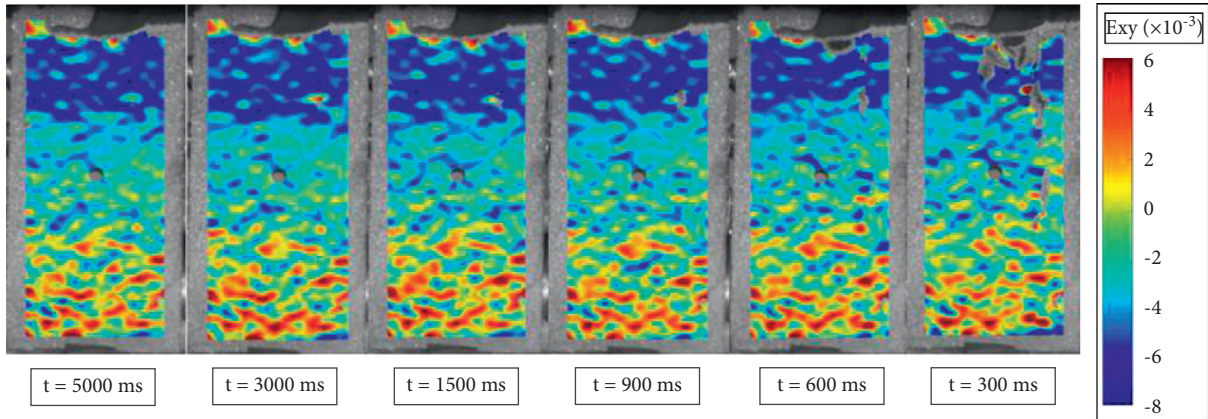


FIGURE 13: Cloud charts of shear strain field evolution of shale sample with hole bedding angle of  $60^\circ$  (where the  $t$  value represents the time before fracturing, red represents positive shear strain and blue represents negative shear strain).

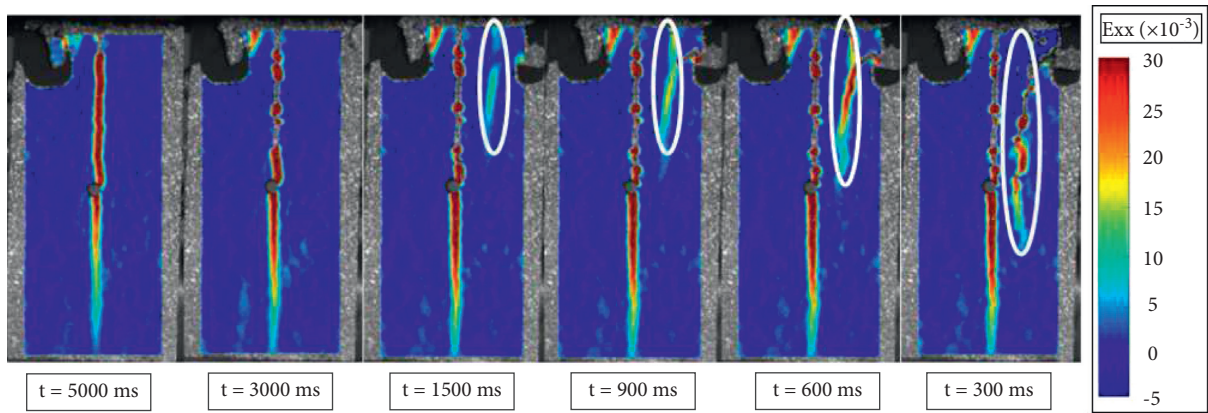


FIGURE 14: Cloud charts of tensile strain field evolution of shale sample with bedding angle of  $90^\circ$  (where the  $t$  value represents the time before fracturing, red represents tensile strain and blue represents compressive strain).

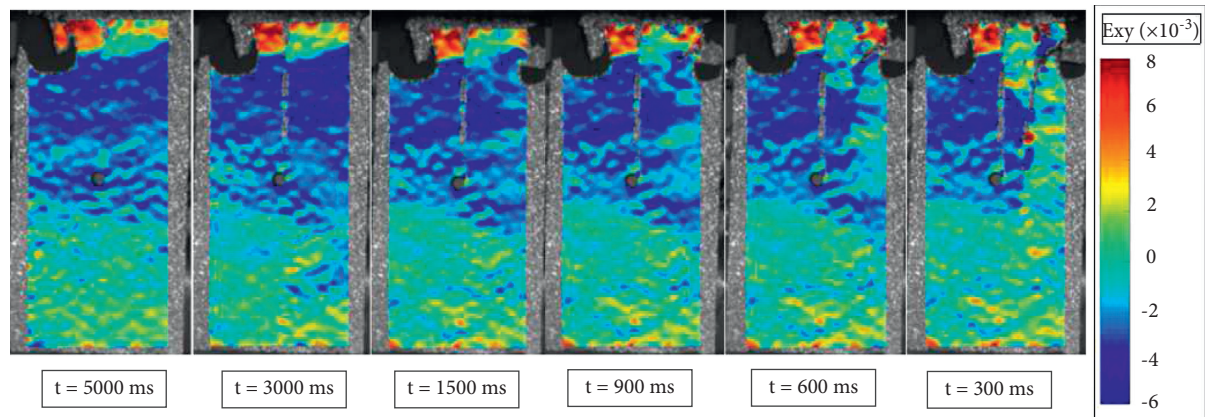


FIGURE 15: Cloud charts of shear strain field evolution of shale sample with hole bedding angle of  $90^\circ$  (where the  $t$  value represents the time before fracturing, red represents positive shear strain and blue represents negative shear strain).

#### 4. Conclusion

In this paper, the influence of bedding angle on the strength characteristics and failure deformation of shale was explored through the uniaxial compression tests combined with DIC.

The results provide theoretical support for the stability of tunnel surrounding rock. The main conclusions are as follows:

- (1) The peak strength of shale with prefabricated circular holes is closely related to bedding dip angle. With the increase of bedding angle, the peak strength first

increases, then dramatically decreases, and finally slightly increases. When the bedding angle is small ( $0^\circ$  and  $15^\circ$ ), the peak strength of the shale mainly depends on the strength of the shale matrix. When the bedding angle is large ( $60^\circ$ ,  $75^\circ$ , and  $90^\circ$ ), the peak strength of shale mainly depends on the strength of the shale bedding plane, and thus, the peak strength is small.

- (2) The global shear strain field of shale with prefabricated circular holes is closely related to the bedding dip angle. When the bedding angle is  $0^\circ$  and  $90^\circ$ , the global shear strain is small. When the bedding dip angle is between  $0^\circ$  and  $90^\circ$ , the global shear strain caused by the joint action of rock internal friction and bedding plane is large, and the global shear strain is the largest when the bedding dip angle is  $30^\circ$  and  $45^\circ$ .
- (3) The failure mode around the circular hole of shale with a prefabricated circular hole is closely related to the bedding dip angle. When the bedding angle is  $0^\circ$ ,  $15^\circ$ ,  $30^\circ$ , and  $45^\circ$ , the failure mode around the circular hole is tension shear mixed failure; When the bedding angle is  $60^\circ$  and  $75^\circ$ , there is no damage around the circular hole. When the bedding angle is  $90^\circ$ , tensile failure occurs around the circular hole.
- (4) The macroscopic crack failure mode of shale with prefabricated circular holes is closely related to the bedding angle. When the bedding angle is  $0^\circ$ ,  $15^\circ$ ,  $30^\circ$ ,  $45^\circ$ , and  $90^\circ$ , the tensile failure runs through the circular holes are mainly produced. When the bedding angle is  $60^\circ$  and  $75^\circ$ , tensile failure away from the circular hole occurs along the weak surface of bedding. [37].

## Data Availability

All data can be obtained from the corresponding author.

## Conflicts of Interest

The authors declare that there are no conflicts of interest.

## Acknowledgments

The authors thank the funding support of the Engineering Research Center of Geothermal Resources Development Technology and Equipment, Ministry of Education, Jilin University (No. 21013), Zhejiang Provincial Natural Science Foundation of China under Grant no. LQ21E040003, and Scientific Research Foundation of Shaoxing University (No. 13011001002/110).

## References

- [1] H. K. Verma, N. K. Samadhiya, M. Singh, R. K. Goel, and P. K. Singh, "Blast induced rock mass damage around tunnels," *Tunnelling and Underground Space Technology*, vol. 71, pp. 149–158, 2018.
- [2] N. Innaurato, R. Mancini, and M. Cardu, "On the influence of rock mass quality on the quality of blasting work in tunnel driving," *Tunnelling and Underground Space Technology*, vol. 13, no. 1, pp. 81–89, 1998.
- [3] V. M. S. R. Murthy and K. Dey, "Predicting overbreak from blast vibration monitoring in a lake tap tunnel—a success story," *Fragblast*, vol. 7, no. 3, pp. 149–166, 2003.
- [4] H. K. Verma, V. V. R. Prasad, and R. K. Goel, "Investigations of rock mass damage induced by blasting in tunnelling," *Journal of Rock Mechanics and Tunnelling Technology*, vol. 22, no. 1, pp. 49–61, 2016.
- [5] K. Dey and V. M. S. R. Murthy, "Determining blast damage envelope through vibration model and validation using seismic imaging," *Mining Technology*, vol. 120, no. 2, pp. 90–94, 2011.
- [6] R. Holmberg, "Design of tunnel perimeter blasthole patterns to prevent rock damage," in *Proceedings of the IMM Tunnelling'79 Conference*, pp. 3–6, London, UK, 1979.
- [7] C. Zhu, M. He, X. Zhang, Z. Tao, Q. Yin, and L. Li, "Nonlinear mechanical model of constant resistance and large deformation bolt and influence parameters analysis of constant resistance behavior," *Rock and Soil Mechanics*, vol. 42, no. 7, pp. 1911–1924, 2021.
- [8] G. Shi, X. Yang, H. Yu, and C. Zhu, "Acoustic emission characteristics of creep fracture evolution in double-fracture fine sandstone under uniaxial compression," *Engineering Fracture Mechanics*, vol. 210, pp. 13–28, 2019.
- [9] C. Zhu, M.-c. He, B. Jiang, X.-z. Qin, Q. Yin, and Y. Zhou, "Numerical investigation on the fatigue failure characteristics of water-bearing sandstone under cyclic loading," *Journal of Mountain Science*, vol. 18, no. 12, pp. 3348–3365, 2021.
- [10] G. Li, Y. Hu, S.-m. Tian, M. weibin, and H.-l. Huang, "Analysis of deformation control mechanism of prestressed anchor on jointed soft rock in large cross-section tunnel," *Bulletin of Engineering Geology and the Environment*, vol. 80, no. 12, pp. 9089–9103, 2021.
- [11] M. Gao, J. Xie, Y. Gao et al., "Mechanical behavior of coal under different mining rates: a case study from laboratory experiments to field testing," *International Journal of Mining Science and Technology*, vol. 31, no. 5, pp. 825–841, 2021.
- [12] M. Gao, H. Hao, S. Xue et al., "Discing behavior and mechanism of cores extracted from Songke-2 well at depths below 4,500 m," *International Journal of Rock Mechanics and Mining Sciences*, vol. 149, Article ID 104976, 2022.
- [13] C. Cao, W. Zhang, J. Chen, B. Shan, S. Song, and J. Zhan, "Quantitative estimation of debris flow source materials by integrating multi-source data: a case study," *Engineering Geology*, vol. 291, Article ID 106222, 2021.
- [14] D. Chen, H. Chen, W. Zhang, J. Lou, and B. Shan, "An analytical solution of equivalent elastic modulus considering confining stress and its variables sensitivity analysis for fractured rock masses," *Journal of Rock Mechanics and Geotechnical Engineering*, vol. 2021, 2021.
- [15] B. Ding, Z. Han, G. Zhang, X. Beng, and Y. Yang, "Flexural toppling mechanism and stability analysis of an anti-dip rock slope," *Rock Mechanics and Rock Engineering*, vol. 54, no. 8, pp. 3721–3735, 2021.
- [16] Z. Dou, S. Tang, X. Zhang et al., "Influence of shear displacement on fluid flow and solute transport in a 3D rough fracture," *Lithosphere*, vol. 2021, Article ID 1569736, 2021.
- [17] Z. Dou, Y. Liu, X. Zhang et al., "Influence of layer transition zone on rainfall-induced instability of multilayered slope," *Lithosphere*, vol. 2021, Article ID 2277284, 2021.

- [18] R. H. C. Wong, P. Lin, and C. A. Tang, "Experimental and numerical study on splitting failure of brittle solids containing single pore under uniaxial compression," *Mechanics of Materials*, vol. 38, no. 1-2, pp. 142-159, 2006.
- [19] D. Li, Q. Zhu, Z. Zhou, X. Li, and P. G. Ranjith, "Fracture analysis of marble specimens with a hole under uniaxial compression by digital image correlation," *Engineering Fracture Mechanics*, vol. 183, pp. 109-124, 2017.
- [20] X. Fan, R. Chen, H. Lin, H. Lai, C. Zhang, and Q. Zhao, "Cracking and failure in rock specimen containing combined flaw and hole under uniaxial compression," *Advances in Civil Engineering*, vol. 2018, Article ID 9818250, 15 pages, 2018.
- [21] H. Wang, A. Dyskin, E. Pasternak, P. Dight, and M. Sarmadivaleh, "Effect of the intermediate principal stress on 3-D crack growth," *Engineering Fracture Mechanics*, vol. 204, pp. 404-420, 2018.
- [22] H. Wang, A. Dyskin, and E. Pasternak, "Comparative analysis of mechanisms of 3-D brittle crack growth in compression," *Engineering Fracture Mechanics*, vol. 220, Article ID 106656, 2019.
- [23] H. Wang, A. Dyskin, E. Pasternak, P. Dight, and M. Sarmadivaleh, "Experimental and numerical study into 3D crack growth from a spherical pore in biaxial compression," *Rock Mechanics and Rock Engineering*, vol. 53, no. 1, pp. 77-102, 2020.
- [24] G. Han, Q. Liang, R. Bao, and Y. Zhou, "Influence of Circular Hole Diameter on Deformation and Failure of Longmaxi Shale," *Geotechnical and Geological Engineering*, vol. 2022, pp. 1-9, 2022.
- [25] Z. Li, S. Liu, W. Ren, J. Fang, Q. Zhu, and Z. Dun, "Multiscale laboratory study and numerical analysis of water-weakening effect on shale," *Advances in Materials Science and Engineering*, vol. 2020, Article ID 5263431, 14 pages, 2020.
- [26] D. Charpentier, D. Tessier, and M. Cathelineau, "Shale microstructure evolution due to tunnel excavation after 100 years and impact of tectonic paleo-fracturing," *Case of Tournemire, France*, *Engineering Geology*, vol. 70, no. 1-2, pp. 55-69, 2003.
- [27] M. Josh, L. Esteban, C. Delle Piane, J. Sarout, D. N. Dewhurst, and M. B. Clennell, "Laboratory characterisation of shale properties," *Journal of Petroleum Science and Engineering*, vol. 88-89, pp. 107-124, 2012.
- [28] V. Ghiasi, H. Omar, J. Rostami et al., "Geotechnical and geological studies of NWCT tunnel in Iran focusing on the stabilization analysis and design of support: a case study," *Scientific Research and Essays*, vol. 6, no. 1, pp. 79-97, 2011.
- [29] Z. Hou, C. Yang, Y. Guo et al., "Experimental study on anisotropic properties of Longmaxi formation shale under uniaxial compression," *Rock and Soil Mechanics*, vol. 36, no. 9, pp. 2541-2550, 2015.
- [30] H. Niandou, J. F. Shao, J. P. Henry, and D. Fourmaintraux, "Laboratory investigation of the mechanical behaviour of Tournemire shale," *International Journal of Rock Mechanics and Mining Sciences*, vol. 34, no. 1, pp. 3-16, 1997.
- [31] Y. Zhang, *Study on Anisotropy of Mechanical Properties of the Shale in West Hubei and East Chongqing*, Southwest University of Science and Technology, Mianyang, China, 2016.
- [32] S. Yin, W. Ding, Y. Sun, X. Wang, M. Zhang, and N. Zhang, "Shale uniaxial compressive failure property and the affecting factors of UCS," *Earth Science Frontiers*, vol. 23, no. 2, pp. 75-95, 2016.
- [33] B. Zhang, H. Ma, X. Tian, and C. Zhou, "Deep layered shale mechanical parameters anisotropy study," *Chinese Journal of Underground Space and Engineering*, vol. 16, no. S2, pp. 634-638, 2020.
- [34] C. Zhao, C. Bao, H. Matsuda, C. Zhao, and J. Tian, "Application of digital image correlation method in experimental research on crack propagation of brittle rock," *Chinese Journal of Geotechnical Engineering*, vol. 37, no. 5, pp. 944-951, 2015.
- [35] J. Blaber, B. Adair, and A. Antoniou, "Ncorr: open-source 2D digital image correlation matlab software," *Experimental Mechanics*, vol. 55, no. 6, pp. 1105-1122, 2015.
- [36] B. He, L. Xie, F. Li, P. Zhao, and Y. Zhang, "Anisotropic mechanism and characteristics of deformation and failure of Longmaxi shale," *SCIENTIA SINICA Physica, Mechanica & Astronomica*, vol. 47, no. 11, Article ID 114611, 2017.
- [37] J. Xie, *Experimental Investigation on Hydraulic Fracture Geometry of Perforated Well in Longmaxi Shale Gas Reservoir*, China University of Geosciences, Wuhan, China, 2019.